

## Article

# Flash Flood Hazard Mapping Using Remote Sensing and GIS Techniques in Southwestern Saudi Arabia

Saad S. Alarifi <sup>1,\*</sup>, Mohamed Abdelkareem <sup>2</sup>, Fathy Abdalla <sup>2</sup> and Mislat Alotaibi <sup>3</sup>

<sup>1</sup> Department of Geology and Geophysics, College of Science, King Saud University, P.O. Box 2455, Riyadh 11451, Saudi Arabia

<sup>2</sup> Geology Department, South Valley University, Qena 83523, Egypt

<sup>3</sup> Department of Geosciences, University of Arkansas, Fayetteville, AR 72704, USA

\* Correspondence: author: ssalarifi@ksu.edu.sa

**Abstract:** Flash flooding is one of the most significant natural disasters in arid/hyperarid regions and causes vast property damage and a large number of deaths. For mitigating and reducing flood risks, data from several remote sensing satellite images—Shuttle Radar Topography Mission (SRTM) Digital Elevation Model (DEM), Landsat 8 Operational Land Imager (OLI), and Tropical Rainfall Measuring Mission (TRMM)—were prepared and combined through a GIS-based multicriteria decision-making technique to test and delineate the flash flood vulnerable areas of Wadi Hali in southwestern Saudi Arabia. Several flash flood thematic layers representing topographic, geomorphic, climatic, and hydrological conditions were prepared, normalized, and combined through a GIS-based analytic hierarchy process (AHP) technique to obtain flash flood hazard zones (FFHs). This method successfully presented a satisfactory output map that revealed six zones of flood risk, and areas of extreme hazard covered about 13% of the entire basin. Landsat 8 band composite 7, 5, and 3 and field data validated the FFHs. This map considered a key requirement for sustaining safe settlements downstream of Wadi Hali. Overall, the integration of remote sensing and GIS techniques revealed significant areas of flash flood zones in an arid region.

**Keywords:** modeling; SRTM; Wadi Hali; runoff; satellite data; risk assessment; flood hazards



check for updates

**Citation:** Alarifi, S.S.; Abdelkareem, M.; Abdalla, F.; Alotaibi, M. Flash Flood Hazard Mapping Using Remote Sensing and GIS Techniques in Southwestern Saudi Arabia. *Sustainability* **2022**, *14*, 14145.

<https://doi.org/10.3390/su142114145>

Academic Editor: Antonio Miguel Martínez-Graña

Received: 24 August 2022

Accepted: 9 October 2022

Published: 29 October 2022

**Publisher's Note:** MDPI stays neutral with regard to jurisdictional claims in published maps and institutional affiliations.



**Copyright:** © 2022 by the authors. Licensee MDPI, Basel, Switzerland. This article is an open access article distributed under the terms and conditions of the Creative Commons Attribution (CC BY) license (<https://creativecommons.org/licenses/by/4.0/>).

## 1. Introduction

Flash flooding is one of the most dangerous kinds of natural hazards. It causes sizable destruction and disruption to human activity, and happens in basins of varied size on all continents that extend to hundreds of square kilometers of localized space. This is due to rapid-onset, high-intensity rainstorms producing sudden and high-velocity flows [1–9], particularly in areas of rugged terrain. The water level reaches its crest very quickly [7], making it difficult to predict by local rapid-response teams and thus leaving little time to issue warnings [10,11]. Therefore, the flash flood is still insufficiently understood in terms of prediction and management. As a result of climate change and other environmental issues, flood catastrophes have become the most common natural hazards. This is because climate change has been recognized worldwide in the last few years to induce floods [12–15]. Therefore, it is critical to have access to reliable and up-to-date information in order to prevent or at least mitigate the impacts of floods. A flood-potential map is one of these crucial sorts of information [16].

In order to provide appropriate solutions for floods and sustainable development and management, several studies have assessed and predicted flood risk using climate conditions, geomorphic and physical characteristics of catchments [5,7,8], soil properties, and land use/cover derived from remote sensing data [9,17,18]. The most utilized elements are physical and natural factors (e.g., elevation, slope, aspect, slope curvature, lithology, topographic position index, and rainfall), hydrological factors (e.g., drainage density, distance

to river, topographic wetness index, and stream power index), and human disturbance factors (e.g., land use and road distance) [19–22].

An essential part of effective land use planning in flood areas and mitigation strategies is flood hazard mapping [18]. This offers easily available maps that allow planners to spatially highlight the most dangerous places, which is crucial for mitigation efforts [23,24]. Predicting and preventing floods is a complicated process, but the occurrence and mapping of areas prone to FFHs can be predicted and partially managed using several methods of remote sensing and GIS techniques [7,25–27]. The analysis of remote sensing data through GIS techniques allows the gathering of different datasets in order to reveal high-risk areas and generate flash flood hazard maps [7,14,28]. The knowledge-driven AHP technique [29], which is based on GIS-weighted overlay analysis, has been successfully applied in modeling different environmental conditions [8,30,31]. The GIS technique can handle large volumes of spatial data for processing and can combine data types to predict and find additional water resources [32]. In this approach, a hierarchical tree with multiple levels is used, and the criteria are separated into several subcriteria. This multicriteria decision-making technique has been used in a number of prediction studies [33,34] to develop a solution to complex choice analysis based on hierarchical ordering criteria [35]. The input data used in this model include information about elevation, slope, topographic wetness index (TWI), stream power index (SPI), curvature, drainage density, depressions, runoff, distance to river, and rainfall.

In arid to semiarid regions, such as Saudi Arabia with hot to extremely hot summers and mild to warm winters [36], rainfall varies temporally and spatially, with infrequent high intensity and sporadic occurrences, causing occasional flash floods that result in considerable damage to highways, human life, property, and dams [24,37]. In 2009 and 2011, during the catastrophic flash floods that impacted the Jeddah area, there was approximately SAR 10 billion worth of flash flood damage [38]. In western Saudi Arabia, where the cities of Mecca and Jeddah are located, rainfall occurs from November to April, although sporadic rainfall events are observed in the transition months of October and May. The region is characterized by high rainfall intensity that leads to flash floods. Running water discharged into the Red Sea through wadi basins can pose a threat to coastal cities, towns, villages, and engineering projects [39]. Hence, flash flood susceptibility maps are useful for assessing potential hazards in residential areas where risk has increased in the last few years [24] due to unplanned settlements and climate change.

Management strategies for flash floods mainly depend on modeling hydrological, climatic, and topographic characteristics of a catchment area to obtain an FFH map to reduce the risk of flooding. Such mapping processes, as well as risk analyses, should be carried out as soon as feasible. Therefore, the aim of the present study is to develop a remote sensing-based model that utilizes a different set of remote sensing data to identify flood-prone areas and thus assist in flood risk management by minimizing/controlling the destructive effects of floods in the study area.

## 2. Study Area

The Wadi Hali basin is a part of the Asir mountains region in southwestern Saudi Arabia that extends between latitudes  $18^{\circ}13'44.36''$  and  $19^{\circ}2'55.39''$  N and longitudes  $41^{\circ}21'18.07''$  and  $42^{\circ}29'47.28''$  E. It covers about  $5222 \text{ km}^2$  with a perimeter of 645 km and is mainly composed of basement rocks. Notable mountains of the study area are Jabal Sawda and Jabal Thirban, and the main residential area is Muhayil city, in the middle of the basin, and Hali, downstream on the Red Sea coast (Figure 1). Wadi Hali in the Southern Tihama plain is one of the largest wadi in the Kingdom of Saudi Arabia. It has a total length of 160 km and an average slope of 17.5 m/km. The Red Sea Hills in southwestern Saudi Arabia are composed largely of Neoproterozoic volcanic–sedimentary rock units of the Arabian–Nubian Shield. The crystalline basement is unconformably overlain by thick sequences of sedimentary formations ranging from Cambrian to recent age. The watersheds collect precipitation from the adjoining Hills and channel the collected runoff

toward the Red Sea and its coastal plain as surface runoff and/or infiltration into the groundwater aquifers [40]. The southwestern region is rich in rainfall compared to other regions of the Kingdom of Saudi Arabia, with average annual precipitation in the range of 400–700 mm/y [41].

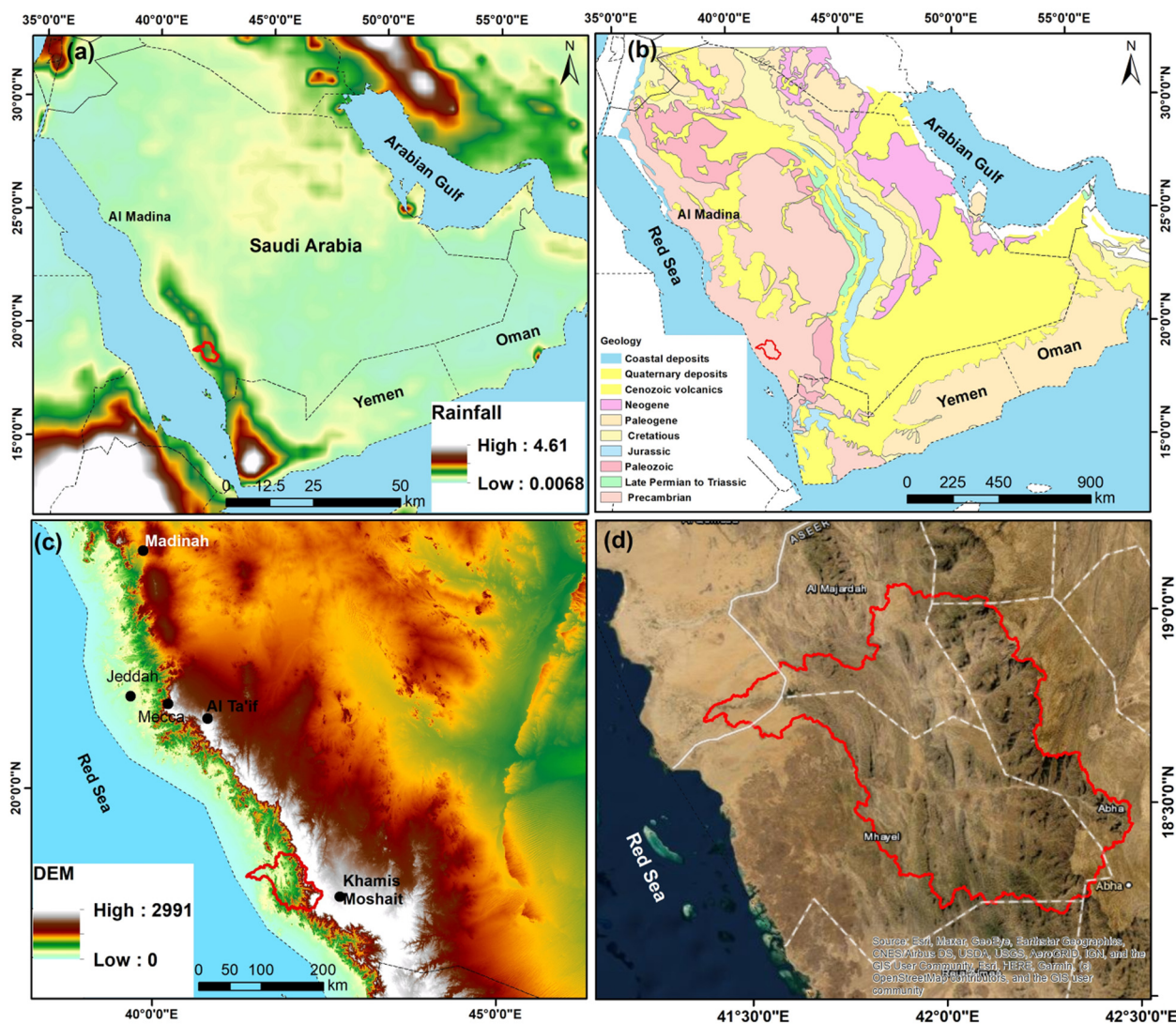


**Figure 1.** Location map of the present study: (a) Rainfall distribution data of Saudi Arabia overlaid by the Wadi Hali watershed; (b) Geological map of Saudi Arabia overlaying the Wadi Hali watershed; (c) DEM of Asir terrain overlaid by the study area; and (d) Wadi Hali watershed on a Geo-Eye1 image.

### 3. Data Used and Methods

Several satellite radar and optical data were collected to characterize the area prone to flash flood hazards in Wadi Hali, west of Saudi Arabia. The Shuttle Radar Topography Mission (SRTM) DEM data were selected to map the topographic characteristics and compute the catchments' parameters. Optical data were also utilized to characterize the land use/cover of the study area (Figure 2).

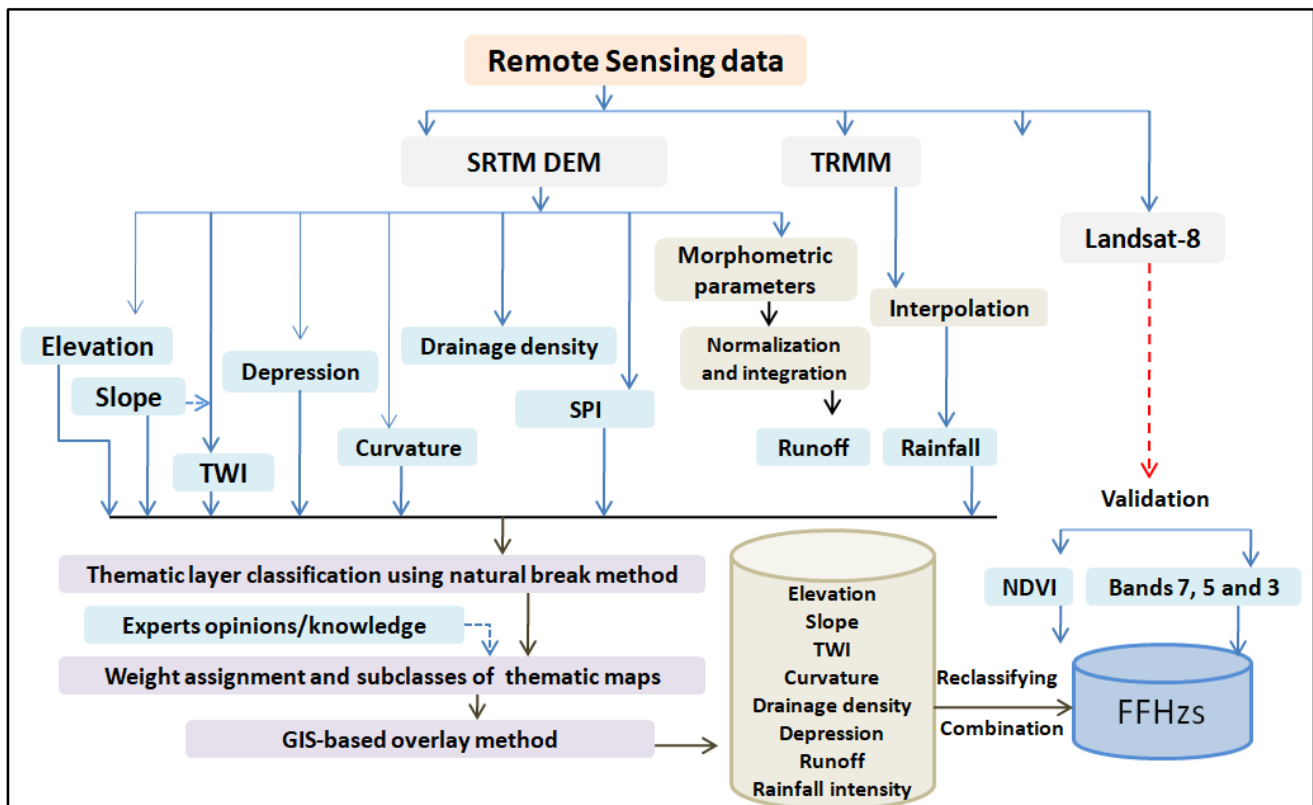


**Figure 2.** Flow chart showing the data and methods adopted in the present study.

The SRTM data (~90 m cell size) were obtained as an international collaboration between NASA, the U.S. National Geospatial-Intelligence Agency, the Italian Space Agency, and the German Aerospace Center. The SRTM DEM data of ~ 90 m spatial resolution are accessible for download from the USGS. They are utilized to delineate the watershed, stream networks, altitude, slope, surface curvature, topographic wetness index (TWI), depressions, Stream Power Index (SPI), stream density, and morphometric parameters using ArcGIS. The D8 method [42] was used to perform the automatic delineation of stream extractions. The stream orders were identified [43,44] and used for calculating other parameters.

The Landsat Operational Land Imager (OLI) optical sensor with 9 spectral bands carried by Landsat 8 was launched on 11 February 2013. Two scenes of Level 1 (path/row 167/047 and path/row 168/047) OLI data were acquired on 14 February 2018. The obtained scenes were mosaicked and linked to the coordinate system of UTM Zone 37 N. The OLI bands 2, 3, 4, 5, 6, and 7 were utilized in this paper to conduct image transformation and enhancement techniques.

The presented GIS-based model is primarily based on elevation parameters, drainage networks, infiltration, and relief along with land use. Mapping FFH susceptible areas need complex datasets to characterize the catchment properties to obtain the output map. The modeling of FFHs requires more information. Such a model is necessary as such an event threatens inhabitants of destroying infrastructures. Global warming places pressure on the global hydrological cycle; therefore, FFHs usually are thought to increase due to global climate change.

In the AHP technique, each layer is assigned a weight [29]. The predictive layers are then compared in a pair-wise comparison matrix (Table 1). Sub-classes of each layer are assigned a weight based on their importance in calculating mineral resources. In this model, the consistency ratio (CR) can be calculated by calculating the Principal Eigen value

( $\lambda$ ), which was calculated using the eigenvector technique, and the Consistency Index (CI), which was calculated using the equation:

$$CI = \frac{(\lambda_{max} - n)}{(n - 1)} \quad (1)$$

**Table 1.** Pairwise comparison matrix, criteria weight, and computed  $\lambda_{max}$ .

	Elev	Slope	Curvature	TWI	SPI	Rainfall	Dep	Dd	DR	Runoff	Criteria Weight	$\lambda_{max}$
Elev	1.0	1.4	2.3	1.4	2.3	1.8	1.8	1.2	1.0	2.3	0.15	10.00
Slope	0.7	1.0	1.7	1.0	1.7	1.3	1.3	0.8	0.7	1.7	0.11	10.00
curvature	0.4	0.6	1.0	0.6	1.0	0.8	0.8	0.5	0.4	1.0	0.06	10.00
TWI	0.7	1.0	1.7	1.0	1.7	1.3	1.3	0.8	0.7	1.7	0.11	10.00
SPI	0.4	0.6	1.0	0.6	1.0	0.8	0.8	0.5	0.4	1.0	0.06	10.00
Rainfall	0.6	0.8	1.3	0.8	1.3	1.0	1.0	0.7	0.6	1.3	0.09	10.00
Dep	0.6	0.8	1.3	0.8	1.3	1.0	1.0	0.7	0.6	1.3	0.09	10.00
Dd	0.9	1.2	2.0	1.2	2.0	1.5	1.5	1.0	0.9	2.0	0.13	10.00
DR	1.0	1.4	2.3	1.4	2.3	1.8	1.8	1.2	1.0	2.3	0.15	10.00
Runoff	0.4	0.6	1.0	0.6	1.0	0.8	0.8	0.5	0.4	1.0	0.06	10.00
Sum	6.7	9.4	15.7	9.4	15.7	11.8	11.8	7.8	6.7	15.7	1.00	100.00

As  $n$  is the number of factors, and max is the major eigenvalue. The RCI is the Random Consistency Index value, which is based on the Saaty's standard [29]. As a result, we may calculate the CR (Table 2) as follows:

$$CR = \frac{CI}{RCI} \quad (2)$$

**Table 2.** Thematic map weights for generating FFHs.

Thematic Layer	Normalized Layer Weight ( $W_i$ )	Detailed Features/Sub-Classes	Rank	Normalized Layer Weight ( $W_i$ )	Area (%)
Elevation (7)	0.149	18–473	5	0.33	36.6
		473–855	4	0.27	29.3
		855–1344	3	0.2	16.55
		1344–1992	2	0.13	10.49
		1992–2991	1	0.07	7.06
Slope (5)	0.106	0–5	1	0.07	32.71
		5 to 15	2	0.13	27.28
		15–25	3	0.2	21.56
		25–30	4	0.27	8.29
		30–66.50	5	0.33	10.16
Drainage density (6)	0.128	0.180–0.719	1	0.07	6.69
		0.719–0.960	2	0.13	17.95
		0.960–1.137	3	0.2	31.26
		1.137–1.311	4	0.27	31.33
		1.311–1.879	5	0.33	12.77

Table 2. Cont.

Thematic Layer	Normalized Layer Weight ( $W_i$ )	Detailed Features/Sub-Classes	Rank	Normalized Layer Weight ( $W_i$ )	Area (%)
Depressions (4)	0.085	0	1	0.25	2.99
		0 to−0.74	3	0.75	97.01
TWI (5)	0.106	3.66–6.71	1	0.1	42.45
		6.71–8.57	2	0.2	32.82
		8.57–11.08	3	0.3	17.65
		11.08–18.92	4	0.4	7.09
		0–1500	1	0.17	97.12
SPI (3)	0.064	1500–5000	2	0.33	1.93
		5000–363,232	3	0.5	0.94
		0.285–0.466	1	0.1	10.04
Rainfall (4)	0.085	0.466–0.586	2	0.2	25.08
		0.586–0.667	3	0.3	41.02
		0.667–0.803	4	0.4	23.86
		6.9–0 (convex)	2	0.33	16.26
Curvature (3)	0.064	0 (flat)	3	0.5	37.8
		0 to−7.09 (concave)	1	0.17	45.93
		26.48 to 28.97	1	0.04761905	2280.985
Runoff (3)	0.064	32.40 to 32.86	2	0.0952381	397.985
		37.42	3	0.14285714	470.156
		43.33	4	0.19047619	336.571
		49.28 to 49.67	5	0.23809524	1224.784
		52.034	6	0.28571429	512.26
		0 to 200	3	0.5	48.18
Distance to River (7)	0.149	200 to 484	2	0.33	36.1
		484 to 1350	1	0.17	15.73

The calculated parameters' CR is 0 ( $CR = 0/1.49$ ) based on this equation, and they are recognized as consistent if the CR is less than 0.1; otherwise, the AHP is meaningless [29].

The score of each sub-feature is standardized to create the sub-feature rating ( $f_i$ ). The FFHs [45] was calculated by multiplying the scores from the previous map by the grade of a thematic map ( $T_i$ ), as illustrated (1):

$$FFHs = \sum_{i=1}^n T_i \times f_i \quad (3)$$

## 4. Results

### 4.1. Factors Influencing Flash Flood Hazards

#### 4.1.1. Elevation

Elevation is frequently used to characterize areas that are liable to FFHs [46,47]. Lower elevation areas are mostly liable to flash floods as lowland areas collect much rainwater [8] and may become flooded quicker as water runs faster from the high elevation to low elevation [47,48] versus areas with a higher elevation that have lower susceptibility. As water drains from the upland of the mountains and links in the lower elevation in the streams. It is often difficult to encounter flooding in areas of high elevation [49,50]. An

elevation map based on SRTM DEM data was then distinguished into five groups, viz., very high, high, moderate, low, and very low (Figure 3a,b and Table 2).

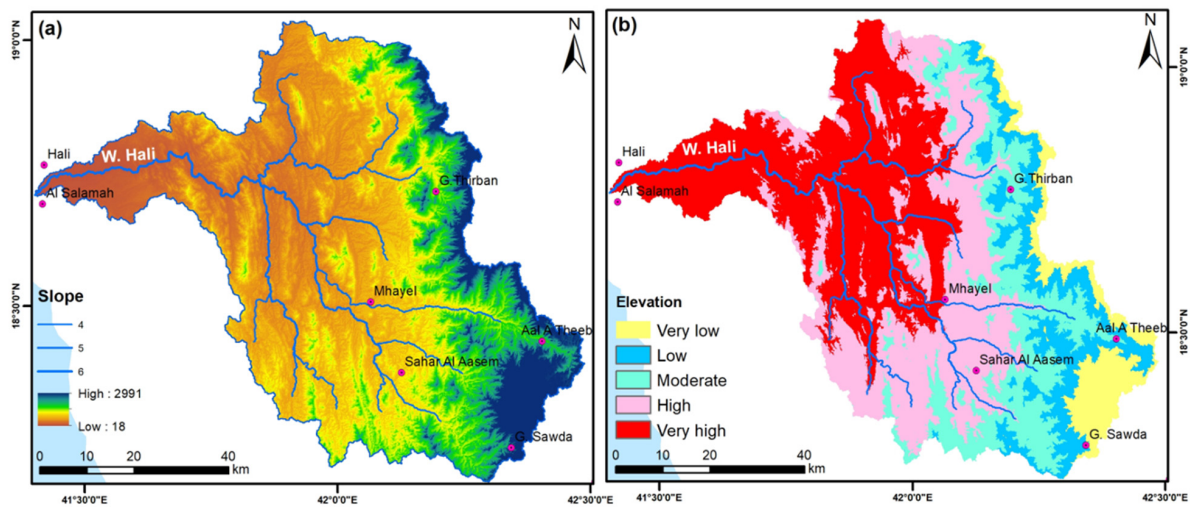


**Figure 3.** (a) Elevation map of Wadi Hali; (b) classified elevation map.

#### 4.1.2. Slope

The slope is the most important index for delineating and characterizing surface runoff and liable area to FFHs due to its indication of the variation in elevations and its right impact on catchments [8,27], speed of runoff, and infiltration capabilities [27,51]. The slope classes with fewer degrees were assigned a higher grade to FFHs [8] as areas of the lower slope are more exposed to flooding [15,48,52]. Flat areas have a high potential for flood occurrence. However, several studies implemented positive relationships between slope and flood susceptibility [7,53,54]. Since the slope angle values increase, the overland flow velocity increases [50]. With increasing the slope degree, the infiltration decreases; hence, there is a larger amount of drained the streams and creating flooding [51]. Therefore, in areas with steep slopes, runoff increases [55].

Based on SRTM DEM, the slope degree map was classified into five classes. Slope angle was grouped into six classes, viz., flat to very low, low, moderate, high, and very high (0–5, 5–15, 15–25, 25–30, and 30–66.50, respectively) (Figure 4a,b and Table 2). In this approach, the slope classes with high degrees were assigned a higher grade to flash flood susceptibility.

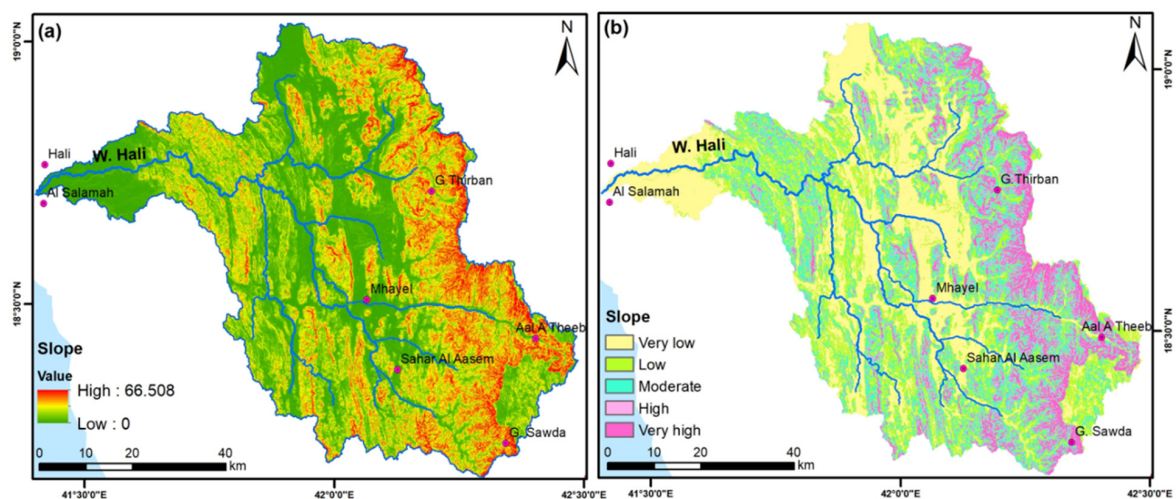


**Figure 4.** (a) Slope degree map; (b) reclassified slope map.

#### 4.1.3. Surface Curvature

Land surface curvature is an important factor connected to the accumulation, infiltration, and runoff on the slope [27,38,56]. The surface curvature layer is derived from the digital elevation model and categorized into three classes: concave (positive values), convex (negative values), and flat (value 0) (Figure 5 and Table 2). Land surface curvature characterizes the areas prone to runoff; in flat areas, water accumulates more easily and these are areas that are susceptible to flash flood hazards [57] than convex and concave areas. Concave areas refer to a low FFH probability, but flat areas are probably more exposed to FFHs.

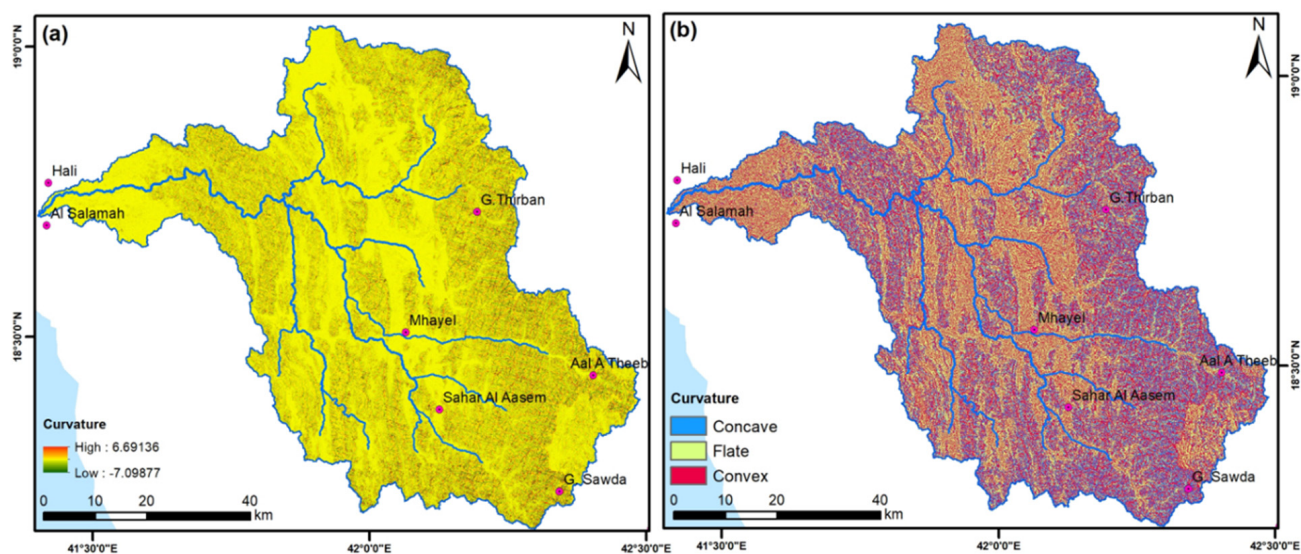


**Figure 5.** (a) Curvature derived from DEM; (b) curvature classes, including concave, flat, and convex.

#### 4.1.4. Topographic Wetness Factor (TWI)

The index of TWI is utilized to evaluate the topographic influence to understand hydrological conditions. TWI refers to the size of flow accumulation at a certain point in the watershed and the tendency of water flow downslope under the force of gravity [58], which accelerates water flow accumulation and, hence, destructive power. This factor can also describe the soil moisture. TWI can be estimated by the below equation:

$$TWI = \ln (Ac/\tan S) \quad (4)$$

where  $Ac$  is the specific catchment area ( $m^2/m$ ) and  $S$  is the slope gradient (in degrees).

The resulting TWI map (Figure 6a) was classified using the natural breaks method into four classes, viz., low, moderate, high, and very high (Figure 6a and Table 2). TWI is positive for FFHs as high values of TWI have a high vulnerability to flooding and lower values of TWI have a lower flood vulnerability [14,15].

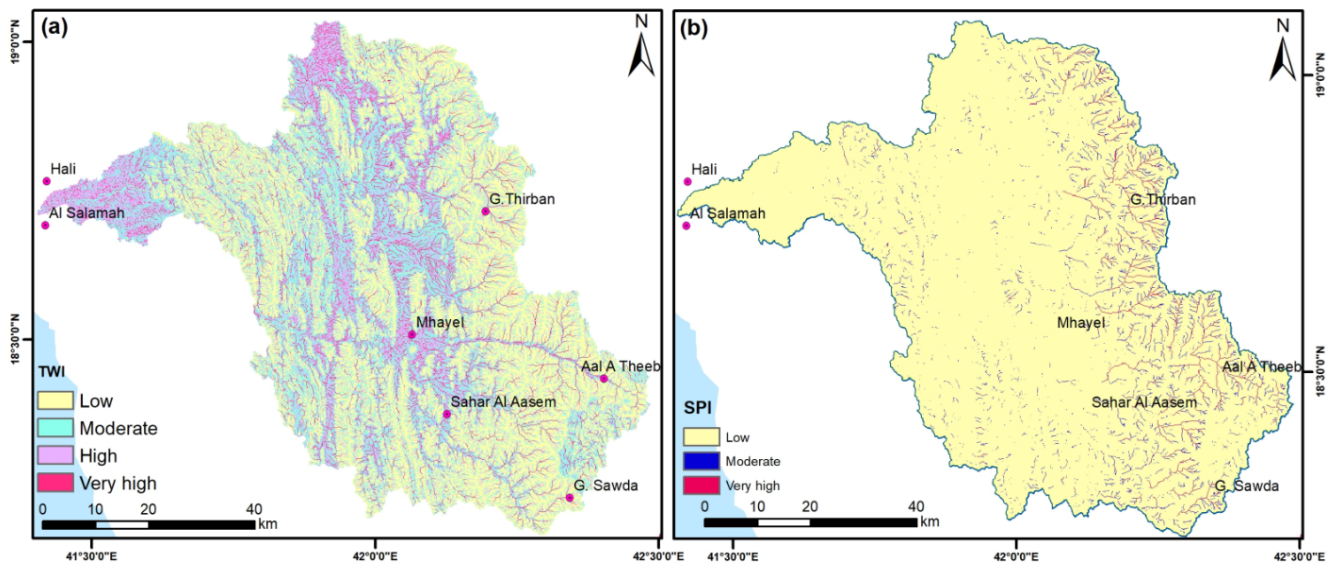


**Figure 6.** (a) TWI is distributed in four classes. (b) SPI is distributed from low to very high.

#### 4.1.5. Stream Power Index (SPI)

Stream power index (SPI) characterizes the potential flow erosion at a certain point on the topographic surface [59]. SPI describes the power of water flow in connection to erosion [59]. The increase in slope gradient and catchment area yield a high amount of water and increase the velocity of water flow that is captured from upslope areas; thus, SPI and erosion risk increase. Using slope and flow accumulation parameters, SPI was computed using Arc GIS software version 10.5. The influence of FFHs increased as the value of SPI increased [57]. In this context, the SPI map is classified into three classes, viz., low, moderate, and high (Figure 6b and Table 2). The stream power index was calculated as follows [60]:

$$\text{SPI} = \text{Ac} * \tan S \quad (5)$$

#### 4.1.6. Rainfall Intensity

Rainfall conditions represent a significant factor in flash flood hazards caused by excessive rainfall in a very short time [61]. Rainfall has a direct relationship to FFHs [8,47,48,62,63]. The average daily precipitated data were collected from the TRMM satellite during the period of 1 January 1998 to 30 November 2013 and interpolated using the inverse distance weighted (IDW) method in GIS to display the precipitation distribution in Wadi Hali (Figure 7a and Table 2). The rainfall intensity map that ranges from 0.285 to 0.803 mm/daily (Figure 7a) is classified into four classes, viz., low, moderate, high, and very high (Figure 7b and Table 2). Spatially, precipitation is common in the maximum elevation in the eastern part, e.g., G. Sawda and G. Thirban, and the urban district of Mhayel area, but it decreases downstream.

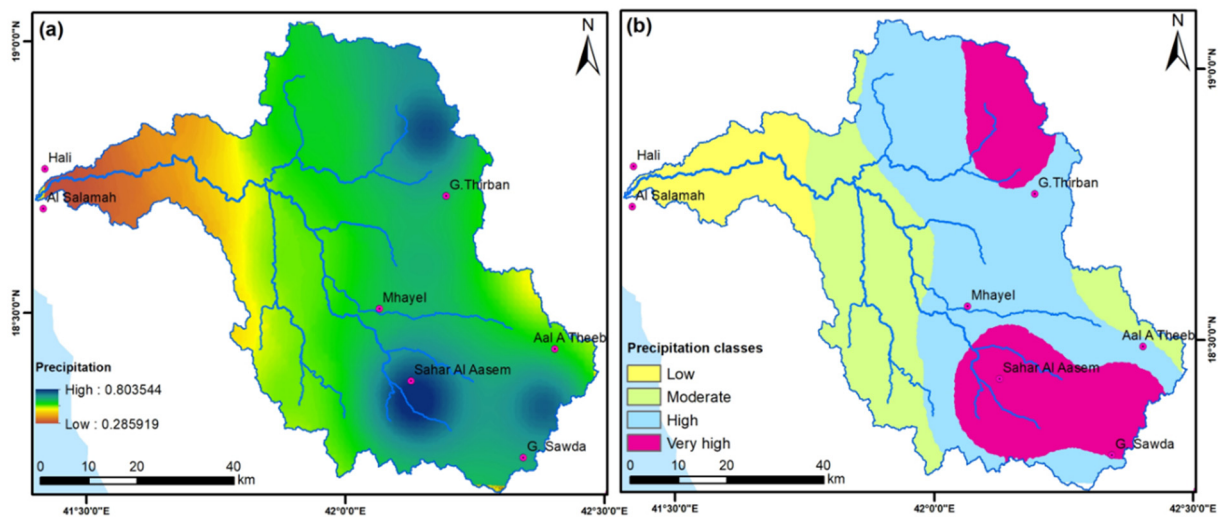


Figure 7. (a) Rainfall map of Wadi Hali; (b) rainfall class map.

#### 4.1.7. Depressions

Depressions are low elevation areas surrounded by high relief and collect, capture, and store precipitated water during runoff of heavy storms in areas of arid/hyperarid climatic conditions. These areas that accumulate water can be inundated by water until it evaporates and infiltrates strata and into inner aquifers [51]. These depressions can be filled with precipitated water until the water elevation reaches a level at which the flow would pour out of the depression. Although these areas are promising for water resources, they are prone to flash flood hazards and present a danger of inundating residential areas. They can be detected in SRTM DEM using spatial analysis with ArcMap v. 10.5. The resulting map can be classified into two classes,  $\geq 0$  (low), and 0 to  $-74$  (high), based on the ability to collect and accumulate precipitated water (Figure 8b and Table 2).

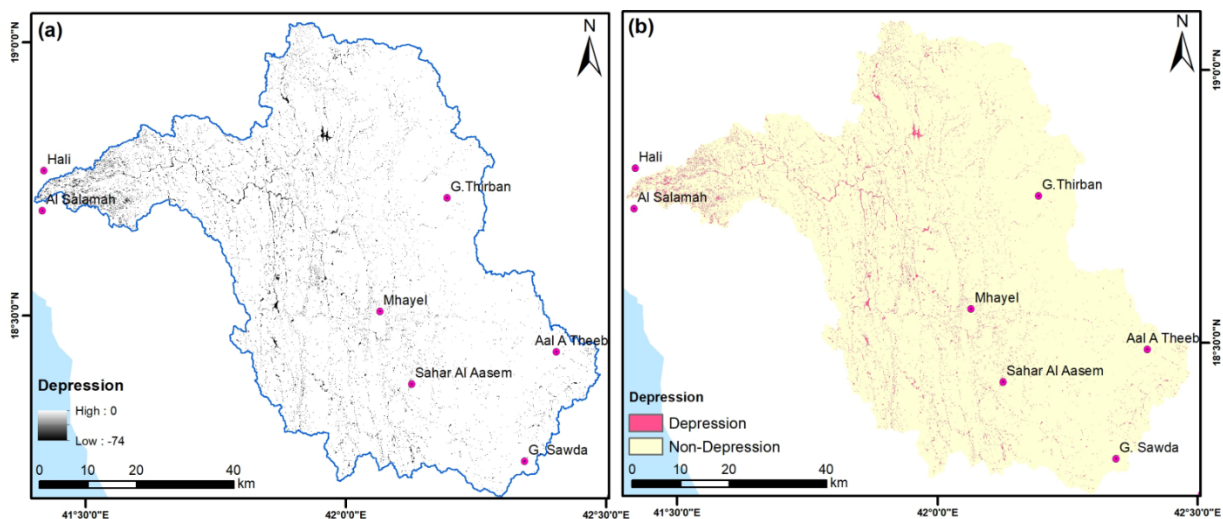
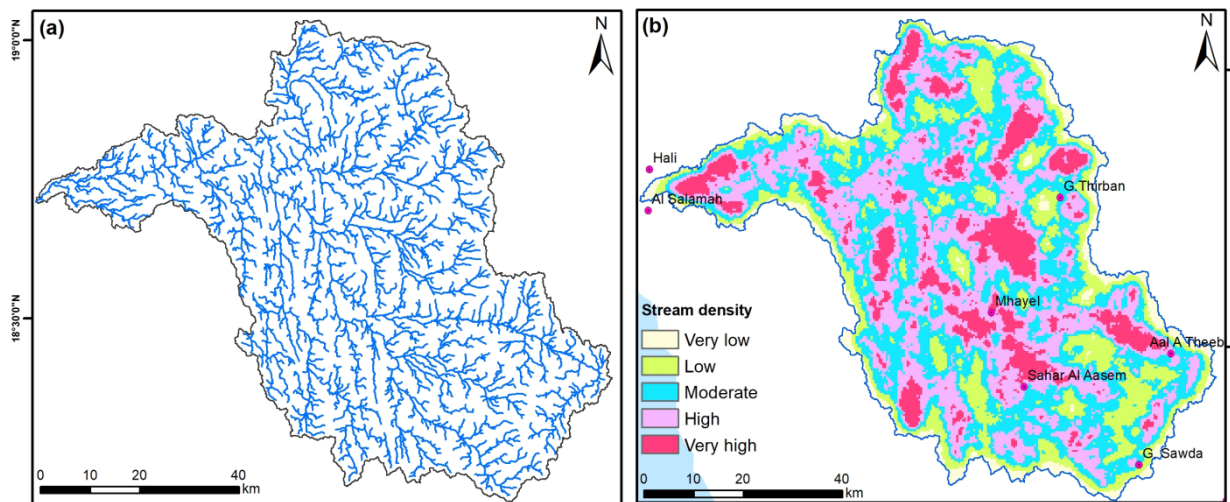


Figure 8. (a) Depression map of Wadi Hali; (b) depression class map.

#### 4.1.8. Drainage Density

Drainage density is computed as the total length per unit area of the stream network (Figure 9, Table 2). Drainage density is negatively correlated to permeability; areas with high Dd are related to surface runoff [55,64]. Drainage density is positively correlated with flooding. The higher susceptibility to flooding is directly correlated to higher drainage

density as it indicates a high surface runoff [6,15,63,65–67]. However, some researchers have assigned a high flash flood susceptibility to low-drainage-density areas [8,68].



**Figure 9.** (a) Drainage networks; (b) drainage density.

#### 4.1.9. Distance to River

The distance to rivers affects the moisture content of soils and rocks on slopes [69]. This factor can affect the recharging process: compared to further distances from river networks, the closer the distance to the river, the greater the chance of infiltration. Based on the DEM of the research region (Figure 10a,b), three groups were created: 0–200, 200–484, and 484–1350 (Table 2).

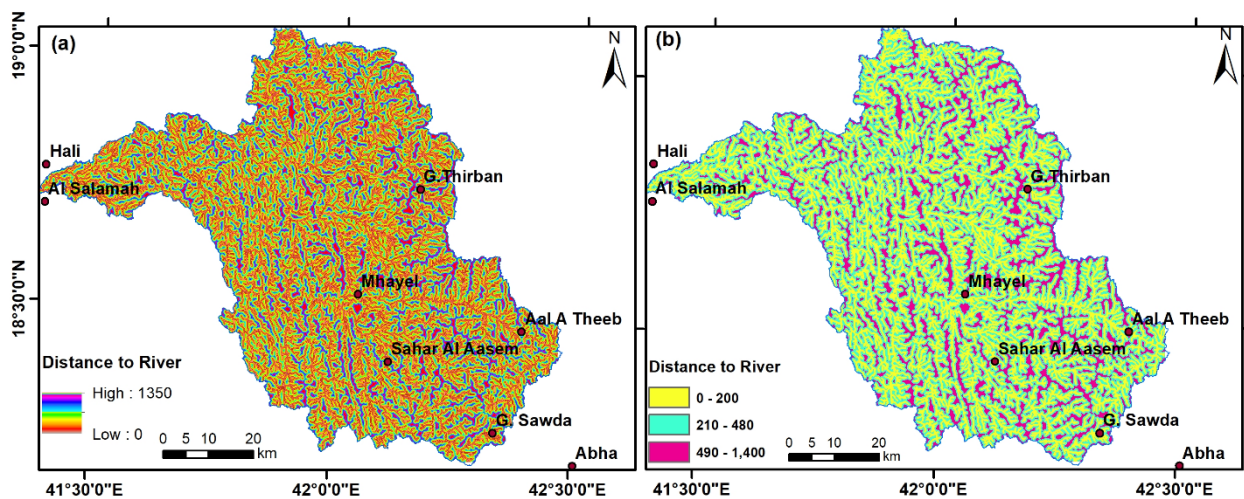


**Figure 10.** (a) Distance to river; (b) classes of the distance to river parameter.

#### 4.1.10. Runoff-Based Morphometric Characteristics

The modeling of flash flood hazards requires the combination of several morphometric indices. The geomorphic characteristics of the catchments are a substantial task in FFHs. The quantitative morphometric characteristics of the catchments are calculated based on the SRTM DEM data [7,51,67] that control the flash flood hazards [65]. The Hali watershed, covering about 5222 km<sup>2</sup> with a perimeter of 645, is sub-divided into 11 sub-basins to delineate the areas prone to flash flood hazards. Based on the analysis of SRTM DEM, the computed twelve quantitative morphometric indices display variations from one sub-basin to another (Figure 11a,b and Table 3).

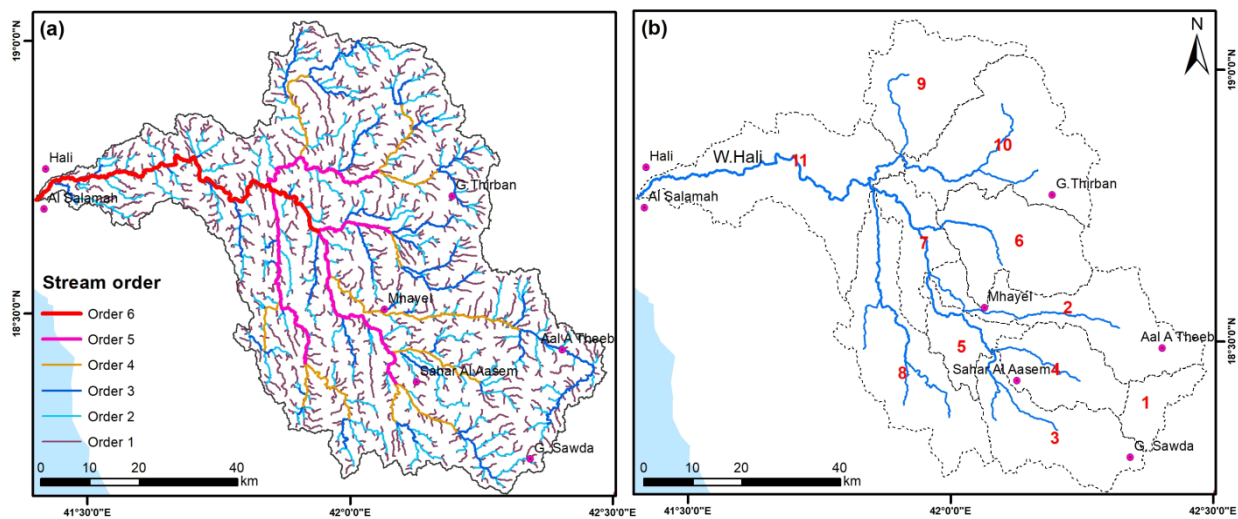


Figure 11. Stream-networks: (a) stream order and (b) Wadi Hali sub-basins.

Table 3. Morphometric analysis of Wadi Hali.

Basin_NO	U	$N_u$	$L_u$	A	P	$L_b$	W	$R_b$	$R_e$	$R_f$	$R_c$	$R_t$	$F_s$	$D_d$	$L_g$	$I_f$	$B_h$	$R_h$	$R_n$
1	4	199	202.745	148.797	89.82	21.722	12.351	3.846	0.634	0.315	0.232	2.216	1.337	1.363	0.367	1.822	1.433	0.066	1.953
2	5	688	787.277	558.568	240.3	58.914	24.146	4.872	0.453	0.161	0.122	2.863	1.232	1.409	0.355	1.736	2.472	0.042	3.484
3	6	643	637.404	470.156	165.6	40.864	16.883	4.505	0.599	0.282	0.215	3.883	1.368	1.356	0.369	1.854	2.498	0.061	3.387
4	6	447	470.783	336.571	118.62	29.921	18.621	4.526	0.692	0.376	0.301	3.768	1.328	1.399	0.357	1.858	2.241	0.075	3.135
5	5	265	285.64	200.726	127.8	28.230	20.168	3.904	0.566	0.252	0.154	2.074	1.320	1.423	0.351	1.879	1.010	0.036	1.437
6	6	667	756.687	512.260	154.08	34.252	26.107	4.487	0.746	0.437	0.271	4.329	1.302	1.477	0.338	1.923	2.524	0.074	3.728
7	5	354	360.188	249.188	133.92	33.506	13.804	4.476	0.532	0.222	0.175	2.643	1.421	1.445	0.346	2.053	0.930	0.028	1.344
8	6	887	990.004	690.323	244.26	61.344	17.609	5.087	0.483	0.183	0.145	3.631	1.285	1.434	0.349	1.843	1.374	0.022	1.970
9	5	655	702.135	481.326	163.08	32.902	23.761	4.775	0.752	0.445	0.227	4.016	1.361	1.459	0.343	1.985	2.326	0.071	3.393
10	6	1029	1050.382	743.459	214.2	40.112	38.863	4.475	0.767	0.462	0.204	4.804	1.384	1.413	0.354	1.955	2.597	0.065	3.669
11	5	1053	1209.444	831.368	266.04	55.065	41.119	5.458	0.591	0.274	0.148	3.958	1.267	1.455	0.344	1.843	1.058	0.019	1.539
WadiHali	6	1472	3600.665	5222.742	645.48	121.541	94.133	4.553	0.671	0.354	0.158	2.280	0.282	0.689	0.725	0.194	2.973	0.024	2.050

The *bifurcation ratio* ( $R_b$ ) of the studied sub-basins ranges from 3.84 to 5.45. Sub-basins # 11 and 8 display the highest values in comparison with sub-basins 1 and 5. The high values of  $R_b$  imply the lowest water flow and the highest infiltration tendency and low flood hazard [7,67,70–72]. Likewise, high values of the *length of overland flow* ( $L_g$ ) promote a low runoff capacity and infiltration [7]. In the Hali basin, the  $L_g$  values extend between 0.33 and 0.72. Sub-basin 11 displays high values and 6 and 9 have low values (Figure 12). Three factors describe the shape of the basin. Based on the work of Schumm [73], the *elongation ratio* ( $R_e$ ) is the relationship between the length of the basin and the diameter of the circle of the same area. Therefore, the  $R_e$  values of the studied sub-basins range from 0.45 to 0.76 and have an average of 0.67 (elongated). The highest values were recorded in # 10 and 9; however, # 2 is the lowest. Three sub-basins (# 6, 9, and 10) have less elongated basins, and sub-basins # 1, 3, 4, 5, 7, and 11 have elongated shapes. However, sub-basins # 2 and 8 are more elongated (Figures 12 and 13) and display low runoff as the  $R_e$  is positively correlated to flash flood hazards. Furthermore, the *circularity ratio*  $R_c$  is based on Miller [74] and is defined as the relationship between the basin area and the area to a circle. The  $R_c$  ranges from 0.12 (sub-basin #2) to 0.30 (sub-basin #4) with an average of 0.158 and refers to non-circular shapes as the circularity is reached at  $R_c = 1$ . Another factor that characterizes the basin shape is the *Form factor* ( $R_f$ ) [75]. The  $R_f$  ranges from 0.16 (sub-basin #2) and 0.46 (sub-basin #10). It is noteworthy that the  $R_f$  average is 0.35 and most of the sub-basins have smaller values that tend towards an elongated shape rather than circularity.

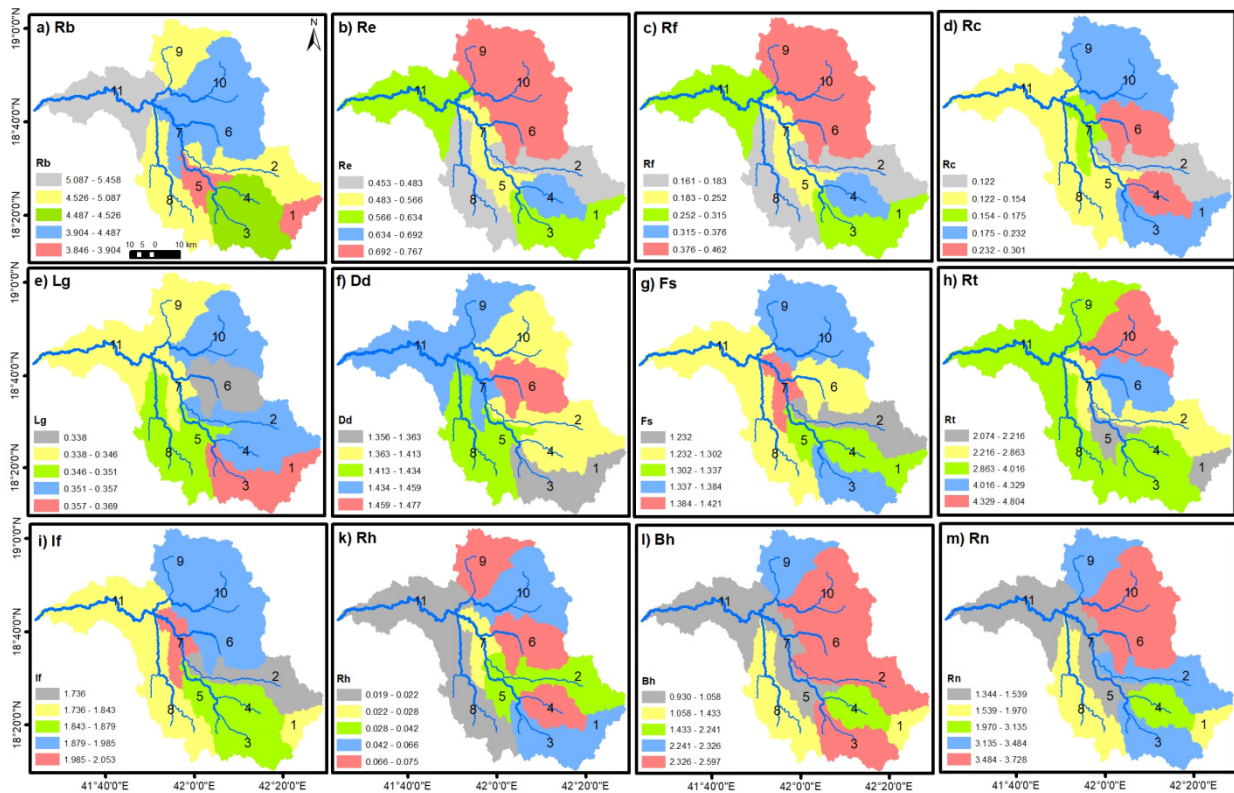


Figure 12. Thematic layers display the computed morphometric parameters (a–i) and (k–m).

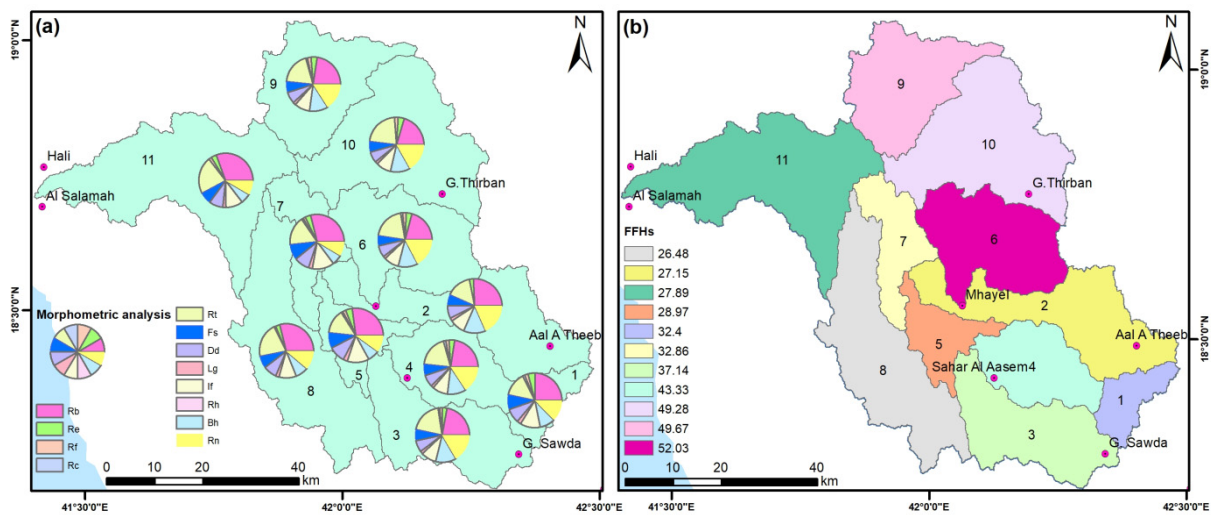


Figure 13. (a) Morphometric indices of Wadi Hali. (b) FFHs based on morphometric indices.

Drainage texture ( $Rt$ ) [73] is very important to estimate the runoff and describes the relationship of stream numbers and the perimeter ( $p$ ) of a selected sub-basin. Therefore,  $Rt$  ranges from 2.074 to 4.80 with an average of 2.280, which implies a moderate texture [7]. In the same context, the stream frequency ( $Fs$ ) [75] ranges from 1.23 (#2) to 1.42 (#7) with an average of 0.282, reflecting low relief [7]. Furthermore, drainage density ( $Dd$ ) is an important indicator that is positive for runoff [7,67]. It ranges from 1.35 (#3) to 1.47 (#6) with an average of 0.68. The infiltration factor ( $If$ ) is computed by multiplying *drainage density* ( $Dd$ ) and *stream frequency* ( $Fs$ ) [76], which implies infiltration capacity and is positively related to runoff. It ranges between 1.73 (#2) and 2.05 (#7) with an average of 0.194.

Basin relief (Bh) describes the differences between the highest elevation and lowest points [43,44], and provides valuable information about runoff. It ranges from 0.93 (#7) to 2.59 (#10) with an average of 2.97. Furthermore, applying *relief ratio* (Rh), which is the product of dividing *basin relief* (Bh) by *basin length* (Lg), offers more information about runoff and slope gradient, as sub-basins with higher Rh reveal high runoff and vice versa [7,51,67]. In the Hali sub-basins, the parameter ranges from 0.019 to 0.074 with an average of 0.024. An additional factor is the ruggedness number (Rn), which reflects the slope and ruggedness of the terrain. It ranges from 1.43 (#5) and 3.72 (#6).

Based on the analysis of the morphometric indices, e.g., Rb and Lg (Table 3) have a negative relationship with flood hazard. However, the rest of the parameters have positive relationships with runoff. Therefore, we applied a linear equation [77] to normalize the data to obtain the flash flood hazard map using morphometric parameters, as follows:

$$\text{Hazard degree} = \frac{4(X - X_{\min})}{(X_{\max} - X_{\min})} + 1 \quad (6)$$

$$\text{Hazard degree} = \frac{4(X - X_{\max})}{(X_{\min} - X_{\max})} + 1 \quad (7)$$

where X represents the value of parameters to be computed for the flood potential of each sub-basin.

Based on computing, normalizing, and combining the obtained morphometric parameters using the above equations and as listed in Table 4, the areas prone to flash flood hazards have higher weights (Figure 13b and Table 4).

**Table 4.** Flash floods hazard degree of Wadi Hali.

Basin_NO	R <sub>b</sub>	L <sub>g</sub>	R <sub>e</sub>	R <sub>f</sub>	R <sub>c</sub>	R <sub>t</sub>	F <sub>s</sub>	D <sub>d</sub>	I <sub>f</sub>	B <sub>h</sub>	R <sub>h</sub>	R <sub>n</sub>	S of Hazard Degree	Hazard Degree
1	5.000	1.244	3.303	3.051	3.462	1.208	3.238	1.225	2.087	2.207	4.359	2.021	32.404	2
2	2.454	2.855	1.000	1.000	1.000	2.157	1.000	2.770	1.000	4.700	2.634	4.590	27.159	1
3	3.367	1.000	2.859	2.602	3.098	3.651	3.878	1.000	2.488	4.762	4.011	4.427	37.142	3
4	3.312	2.497	4.044	3.856	5.000	3.483	3.041	2.418	2.533	4.146	5.000	4.004	43.333	4
5	4.856	3.301	2.446	2.208	1.735	1.000	2.874	3.217	2.798	1.192	2.190	1.156	28.973	1
6	3.410	5.000	4.727	4.662	4.342	4.304	2.490	5.000	3.361	4.825	4.913	5.000	52.034	6
7	3.438	4.020	2.004	1.811	2.185	1.835	5.000	3.955	5.000	1.000	1.614	1.000	32.862	2
8	1.921	3.660	1.390	1.299	1.533	3.282	2.126	3.582	2.344	2.065	1.229	2.051	26.482	1
9	2.694	4.437	4.814	4.768	3.365	3.846	3.734	4.394	4.139	4.350	4.698	4.437	49.676	5
10	3.441	2.967	5.000	5.000	2.834	5.000	4.226	2.881	3.765	5.000	4.271	4.901	49.285	5
11	1.000	4.313	2.758	2.504	1.582	3.761	1.738	4.262	2.343	1.307	1.000	1.327	27.896	1

## 5. Flash Flood Hazard Map

The obtained FFH map, which was produced using an integrated model using inputs from remote sensing data through the GIS analysis tool, was created from ten predictor maps. The input predictors that were employed in building the FFH map are elevation, slope, curvature, TWI, SPI, drainage density, depressions, and rainfall. The FFHs were obtained using a multicriteria GIS-based overlay process of the thematic layers as each cell in a GIS layer fitting to the same pixel location. Thus, the predictor maps were assigned ranks up to 4, and the sub-class features from 1 to 5 (Table 4) that were normalized before synergy. This approach estimates the average ranked multiplied predictor layers. The FFHs were obtained using the following equation:

$$\text{FFHs} = \sum_{i=1}^n W_i \times S_i$$

where  $W_i$  indicates the normalized rank of a predictor of the  $i$  parameter and  $S_i$  is related to the weight of the sub-features.

The FFH map (Figure 14) is grouped into six areas prone to FFHs, extreme, very high, high, moderate, low, and very low, covering 12.85%, 17.42%, 19.20%, 19.28%, and 23.63%, and 7.62%, respectively. Based on the FFH map, the zones from extreme to very high FFHs occupy the areas around the main streams, about 30%. It is noteworthy that the residential

area in Mhayel city is in the zone of very high FFHs (Figure 14c) as is the depression north of the Mhayel city (Figure 14d,e).

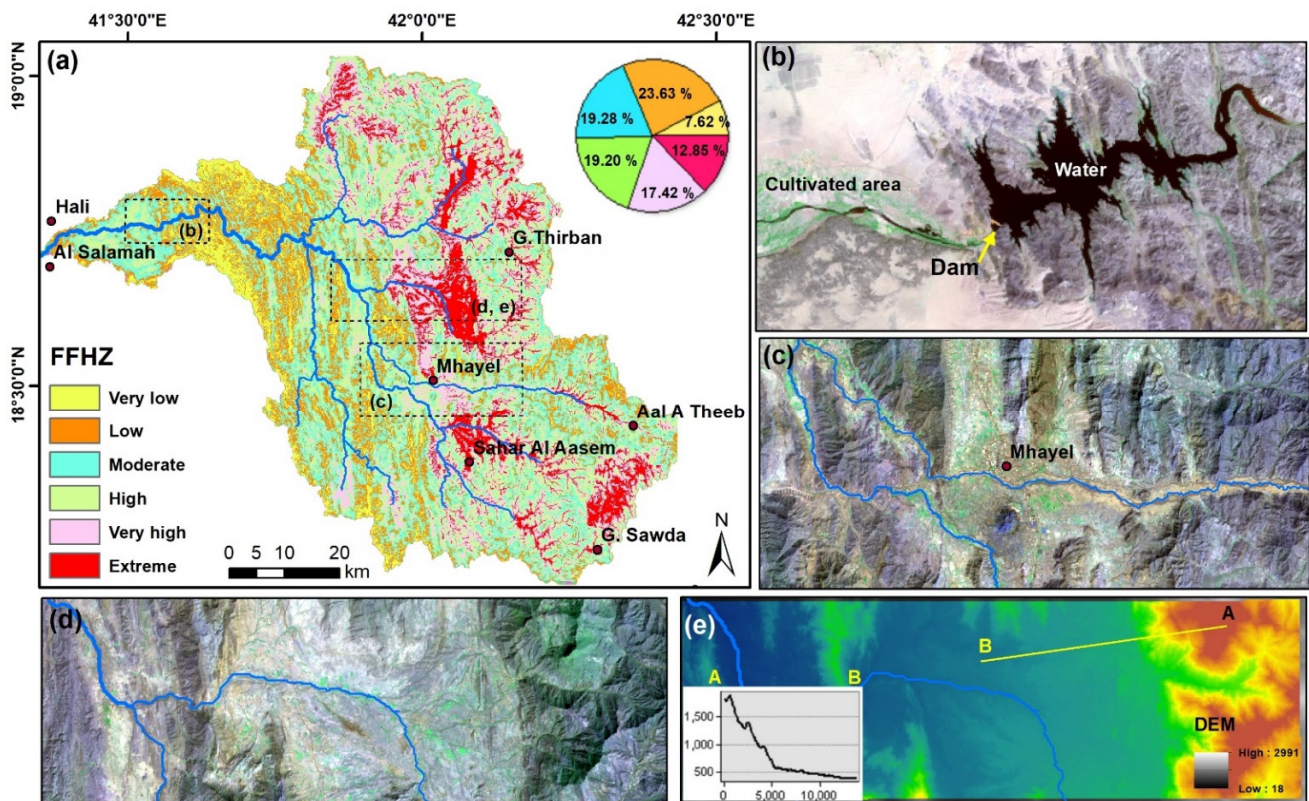


**Figure 14.** (a) Flash flood hazard map of Wadi Hali; (b) Landsat 8 band composite 7, 5, and 3 showing water in dark signatures and vegetation in green; (c) Landsat 8 reveals the Mhayel area in the direction of drainage and covered by vegetation; (d) Subset of Landsat 8 of an area north of Mhayel city displaying high FFHs as depicted in inset “a”; (e) DEM of the same area as in inset “d” overlaid by a topographic profile A–B.

## 6. Discussion

Based on the analysis of different datasets of the geology, topography, hydrology, and climate conditions of Wadi Hali, the area witnessed flash flood hazards. A number of factors influence the incidence of floods in a watershed and the defining flood catchment regions were modeled, revealing that ~13% of the basin is under extreme flood hazard (Figure 14a). The basin is in a rugged terrain and, annually, receives more than 60% of the amount of floods that affect the kingdom, approximately 1250 million cubic meters [78]. Hence, flash flood hazards in the western part of Saudi Arabia are caused by such extreme rainfall events in areas of rugged terrain and hydrological conditions that yield fast runoff and discharge capacity [8,18,79]. The higher the runoff, the more positive the impact on FFHs and the more rapid the response to overland flow, causing the occasional flash floods with considerable damage to highways, human life, property, and dams [37]. In such a region, flash floods significantly affect cities, particularly the western part, causing high losses of properties hazardous mud flows, landslides, and land subsidence [80]. Therefore, they are currently considered as a major geohazard as revealed in the residential areas of Mhayel city in the Wadi Hali basin.

Areas that are densely inhabited, such as Mhayel city, are of high vulnerability; thus, flood mapping and monitoring process, including flooded area extraction and estimation, are important to prevent damages to residential areas and infrastructures [7]. The stream networks of the Wadi Hali basin (Figures 7 and 11) receive sizable, precipitated water within a short time after the onset of rainfall events in the most elevated areas in the

southeast (Figures 3b and 11). Impermeable surfaces, steep slopes, rugged terrains, and high topographic relief yield high runoff (Figure 14a). It is a very challenging issue to manage flash floods as they are related to the climate and topography [27].

Although rainfall intensity causes flash flood in the studied region, it is the principal source of water in addition to the main recharge resource of groundwater aquifers. The amount of vertical infiltration from this running water is a major source of groundwater recharge, which is hydraulically connected [81]. Groundwater recharge volume is important as it depends on the soil infiltration capacity as well as the wadi geometrical and hydraulic variables [51]. The effective use of recharging facilities, especially dams, may promote the enhancement of water infiltration into surficial aquifers, improve the recharge efficiency, and prevent running water from discharging into the Red Sea [78]. According to the results from the field infiltration tests carried out by Abdalla et al. [78], the clear variability of soil infiltration properties is due to the nature of the soil's mechanical composition and soil texture. Coastal plain soils are mostly of a sandy texture (in the upstream part of the wadi), while pediplain and lava field volcanic hill soils are mostly of a fine texture, with a high proportion of pebbles and stones that impede the movement of water in the soil (in the downstream part of the wadi).

The effective beneficiation of rainwater is achieved by constructing dams, especially at the narrow parts of the gentle slope courses within the Wadi Hali basin. These measures include the retardation dams that retain and mitigate running water velocity. Moreover, embankment dams, which are known as flood retention or multifunctional dams, should be constructed to form a zigzag path for the courses of floods. Such a system will assist in the optimum utilization of flood water, preventing severe flash floods and soil erosion, in addition to maximizing and promoting groundwater recharge and raising the water level in the wells below the dam to compensate for the excessive lack of farmers in the surrounding areas, as well as preventing running water from discharging into the Red Sea. The Landsat 8 band composite 7, 5, and 3 show the collected water behind a dam in dark signatures and vegetation in green downstream of Wadi Hali. Such collected rainfall water is extremely important in sustainable development.

The Kingdom of Saudi Arabia intends to construct 31 dams, which will raise the number of dams to 552 to increase the harvest of torrents from 2.3 BCM to 2.57 BCM. These dams work to harvest rainwater, control flood waters and avoid torrential risks, enhance renewable water sources in addition to enhancing groundwater recharge, contribute to achieving water and food security for the Kingdom, and protect lives and property from the dangers of torrential rains and floods. The Hali Dam in the Al Qunfudah Province in the Makkah region is a concrete dam type with four discharging gates (Figure 15a), and is considered the second largest dam in the Kingdom after the King Fahad Dam ( $325,000,000 \text{ m}^3$ ), with a total storage of  $250,000,000 \text{ m}^3$ . The Dam is 384 m in length, 95 m in height and 71 m in width at the base, and 8 m in width at the top crest. The dam was completed and entered service in 2009 to control flood waters and prevent the running water from discharging into the Red Sea by storing it for irrigation and other municipal purposes (Figure 15b–d). The dam helps to secure drinking water supplies for the cities of Makkah, Al Qunfudah, Al-Leith, and Mahayel Asir, with a total production capacity of  $100,000 \text{ m}^3/\text{d}$  and a total capacity of  $36,500,000 \text{ m}^3/\text{a}$ .



**Figure 15.** (a) Hali Dam. (b) Floods in Wadi Hali in 2008 before the construction of the dam. (c) Cultivation in Wad Hali. (d) Hali Dam gates open to stimulate tourism activities.

## 7. Conclusions

In this article, Wadi Hali, which covers a  $\sim 5222 \text{ km}^2$  area, was the object of testing using remote sensing data to map susceptible areas to flash flood hazards (FFHs). Several evidential factors that are frequently utilized in modeling flash flood hazards, including elevation, slope, topographic wetness index (TWI), Stream Power Index (SPI), curvature, drainage density, distance to river, and rainfall intensity, were included in the FFH model. In addition, the present study provided two additional layers to enhance the FFH model, depressions and runoff layers, which are significant to delineate the susceptible areas to flooding and inundation. The runoff layer was derived from the quantitative computation and normalization of twelve morphometric parameters of the eleven sub-basins forming Wadi Hali through a linear equation. The used factors were prepared and combined through a GIS-based statistical AHP coupled with a multicriteria decision analysis technique to map the flash flood prone areas. The relative importance and weights of these factors were calculated. The resultant FFH model successfully revealed six hazard zones, classifying the Wadi Hali basin into extreme (12.85%), very high (17.42%), high (19.20%), moderate (19.28%), low (23.63%), and very low hazards (7.62%). It is concluded that this study revealed that many residential areas in Mhayel and Sahar Al Aasem are susceptible to flood hazards. The results suggested that erecting dams is significant to harvest rainwater, control flood waters and avoid torrential risks, and enhance renewable water sources in addition to enhancing groundwater recharging. The findings enhance our understanding of the relationships between flash flood conditions and the influential geomorphic, hydrologic, topographic, and climatic factors. Overall, the study showed that the adopted remote sensing and GIS techniques are reliable and cost-effective, and could potentially be applied to identify potential risk locations to protect local settlers, support planners, and improve disaster response services during intense rainfall conditions.

**Author Contributions:** Conceptualization, M.A. (Mohamed Abdekareem), F.A. and M.A. (Mislal Alotaibi); funding acquisition, S.S.A.; investigation, S.S.A., M.A. (Mohamed Abdekareem), F.A. and M.A. (Mislal Alotaibi); methodology, S.S.A., M.A. (Mohamed Abdekareem), F.A. and M.A. (Mislal Alotaibi); writing—review and editing, S.S.A., M.A. (Mohamed Abdekareem), F.A. and M.A. (Mislal Alotaibi). All authors have read and agreed to the published version of the manuscript.

**Funding:** This research was funded by King Saud University, grant number RSP2022R496. The APC was funded by King Saud University.

**Institutional Review Board Statement:** Not applicable.

**Informed Consent Statement:** Not applicable.

**Acknowledgments:** This research was supported by the Researchers Supporting Project (RSP2022R496), King Saud University, Riyadh, Saudi Arabia.

**Conflicts of Interest:** The authors declare no conflict of interest.

## References

- Schanze, J. Food Risk Management—A Basic Framework. In *Flood Risk Management: Hazards, Vulnerability and Mitigation Measures*; Schanze, J., Zeman, E., Marsalek, J., Eds.; Springer: Berlin/Heidelberg, Germany, 2006; pp. 1–20.
- Şen, Z.; Khiyami, H.; Al-Harthy, S.; Al-Ammawi, F.; Al-Balkhi, A.; Al-Zahrani, M.; Al-Hawsawy, H. Flash flood inundation map preparation for wadis in arid regions. *Arab. J. Geosci.* **2013**, *6*, 3563–3572. [[CrossRef](#)]
- Doocy, S.; Daniels, A.; Packer, C.; Dick, A.; Kirsch, T.D. The human impact of earthquakes: A historical review of events 1980–2009 and systematic literature review. *PLoS Curr.* **2013**, *5*, 1–9. [[CrossRef](#)] [[PubMed](#)]
- Abdalla, F.; El Shamy, I.; Bamousa, B.; Mansour, M.; Mohamed, A.; Tahoon, M. Flash Floods and Groundwater Recharge Potentials in Arid Land Alluvial Basins, Southern Red. Sea Coast, Egypt. *Int. J. Geosci.* **2014**, *5*, 971–982. [[CrossRef](#)]
- Zhang, D.; Quan, J.; Zhang, H. Flash flood hazard mapping: A pilot case study in Xiapu River Basin, China. *Water Sci. Eng.* **2015**, *8*, 195–204. [[CrossRef](#)]
- Elkhrachy, I. Flash Flood Hazard Mapping Using Satellite Images and GIS Tools: A case study of Najran City, Kingdom of Saudi Arabia (KSA). *Egypt. J. Remote Sens. Space Sci.* **2015**, *18*, 261–278. [[CrossRef](#)]
- Abdelkareem, M. Targeting flash flood potential areas using remotely sensed data and GIS techniques. *Nat. Hazards J.* **2017**, *85*, 19–37. [[CrossRef](#)]
- Waqas, H.; Lu, L.; Tariq, A.; Li, Q.; Baqa, M.F.; Xing, J.; Sajjad, A. Flash Flood Susceptibility Assessment and Zonation Using an Integrating Analytic Hierarchy Process and Frequency Ratio Model for the Chitral District, Khyber Pakhtunkhwa, Pakistan. *Water* **2021**, *13*, 1650. [[CrossRef](#)]
- Abdelkareem, M.; Al-Arifi, N. The use of remotely sensed data to reveal geologic, structural, and hydrologic features and predict potential areas of water resources in arid regions. *Arab. J. Geosci.* **2021**, *14*, 1–15. [[CrossRef](#)]
- Collier, C.G. Flash flood forecasting: What are the limits of predictability? *Q. J. Meteorol. Soc.* **2007**, *133*, 3–23. [[CrossRef](#)]
- Carpenter, T.M.; Sperflage, J.A.; Georgakakos, K.P.; Sweeney, T.; Fread, D.L. National threshold runoff estimation utilizing GIS in support of operational flash flood warning systems. *J. Hydrol.* **1999**, *224*, 21–44. [[CrossRef](#)]
- Charlton, R.; Fealy, R.; Moore, S.; Sweeney, J.; Murphy, C. Assessing the impact of climate change on water supply and flood hazard in Ireland using statistical downscaling and hydrological modeling techniques. *Clim. Chang.* **2006**, *74*, 475–491. [[CrossRef](#)]
- Scheuer, S.; Haase, D.; Volk, M. Integrative assessment of climate change for fast-growing urban areas: Measurement and recommendations for future research. *PLoS ONE* **2017**, *12*, e0189451. [[CrossRef](#)] [[PubMed](#)]
- Khosravi, K.; Pourghasemi, H.R.; Chapi, K.; Bahri, M. Flash flood susceptibility analysis and its mapping using different bivariate models in Iran: A comparison between Shannon’s entropy, statistical index, and weighting factor models. *Environ. Monit. Assess.* **2016**, *188*, 1–21. [[CrossRef](#)] [[PubMed](#)]
- Ullah, K.; Zhang, J. GIS-based flood hazard mapping using relative frequency ratio method: A case study of Panjkora River Basin, eastern Hindu Kush, Pakistan. *PLoS ONE* **2020**, *15*, e0229153. [[CrossRef](#)]
- Papaioannou, G.; Efstratiadis, A.; Vasiliades, L.; Loukas, A.; Papalexioiu, S.M.; Koukouvinos, A.; Tsoukalas, I.; Kossieris, P. An operational method for flood directive implementation in ungauged urban areas. *Hydrology* **2018**, *5*, 24. [[CrossRef](#)]
- Rahmati, O.; Darabi, H.; Haghghi, A.T.; Stefanidis, S.; Kornejady, A.; Nalivan, O.A.; Tien Bui, D. Urban flood hazard modeling using self-organizing map neural network. *Water* **2019**, *11*, 2370. [[CrossRef](#)]
- Hong, Y.; Abdelkareem, M. Integration of remote sensing and a GIS-based method for revealing prone areas to flood hazards and predicting optimum areas of groundwater resources. *Arab. J. Geosci.* **2022**, *15*, 1–14. [[CrossRef](#)]
- Al-Juaidi, A.E.; Nassar, A.M.; Al-Juaidi, O.E. Evaluation of flood susceptibility mapping using logistic regression and GIS conditioning factors. *Arab. J. Geosci.* **2018**, *11*, 765. [[CrossRef](#)]
- Zhao, G.; Pang, B.; Xu, Z.; Yue, J.; Tu, T. Mapping flood susceptibility in mountainous areas on a national scale in China. *Sci. Total Environ.* **2018**, *615*, 1133–1142. [[CrossRef](#)]

21. Darabi, H.; Choubin, B.; Rahmati, O.; Haghighi, A.T.; Pradhan, B.; Kløve, B. Urban flood risk mapping using the GARP and QUEST models: A comparative study of machine learning techniques. *J. Hydrol.* **2019**, *569*, 142–154. [[CrossRef](#)]
22. Costache, R. Flash-flood potential index mapping using weights of evidence, decision trees models and their novel hybrid integration. *Stoch. Environ. Res. Risk Assess.* **2019**, *33*, 1375–1402. [[CrossRef](#)]
23. Billi, P.; Alemu, Y.T.; Ciampalini, R. Increased frequency of flash floods in Dire Dawa, Ethiopia: Change in rainfall intensity or human impact? *Nat. Hazards* **2015**, *76*, 1373–1394. [[CrossRef](#)]
24. Bathrellos, G.D.; Karymbalis, E.; Skilodimou, H.D.; Gaki-Papanastassiou, K.; Baltas, E.A. Urban flood hazard assessment in the basin of Athens Metropolitan city, Greece. *Environ. Earth Sci.* **2016**, *75*, 319. [[CrossRef](#)]
25. Malik, S.; Pal, S.C. Application of 2D numerical simulation for rating curve development and inundation area mapping: A case study of monsoon dominated Dwarakeswar River. *Int. J. River Basin Manag.* **2020**, *18*, 1–11. [[CrossRef](#)]
26. Wang, Y.; Hong, H.; Chen, W.; Li, S.; Pamucar, D.; Gigovic, L.; Drobnjak, S.; Tien Bui, D.; Duan, H. A hybrid GIS multi-criteria decision-making method for flood susceptibility mapping at Shangyou, China. *Remote Sens.* **2018**, *11*, 62. [[CrossRef](#)]
27. Yariyan, P.; Janizadeh, S.; Van Phong, T.; Nguyen, H.D.; Costache, R.; Van Le, H.; Pham, B.T.; Pradhan, B.; Tiefenbacher, J.P. Improvement of Best First Decision Trees Using Random subspace and Dagging Ensembles for Flood Probability Mapping. *Water Resour. Manag.* **2020**, *34*, 1–17. [[CrossRef](#)]
28. Vojtek, M.; Vojteková, J. Flood susceptibility mapping on a national scale in Slovakia using the analytical hierarchy process. *Water* **2019**, *11*, 364. [[CrossRef](#)]
29. Saaty, T.L. *The Analytic Hierarchy Process: Planning, Priority Setting, Resource Allocation*; McGraw-Hill: New York, NY, USA, 1980.
30. Abdelkareem, M.; Al-Arifi, N.; Abdalla, F.; Mansour, A.; El-Baz, F. Fusion of Remote Sensing Data Using GIS-Based AHP-Weighted Overlay Techniques for Groundwater Sustainability in Arid Regions. *Sustainability* **2022**, *14*, 7871. [[CrossRef](#)]
31. Danumah, J.H.; Odai, S.N.; Saley, B.M.; Szarzynski, J.; Thiel, M.; Kwaku, A.; Kouame, F.K.; Akpa, L.U. Flood risk assessment and mapping in Abidjan district using multi-criteria analysis (AHP) model and geoinformation techniques, (cote d’ivoire). *Geoenviron. Disasters* **2016**, *3*, 10. [[CrossRef](#)]
32. Yin, H.; Shi, Y.; Niu, H.; Xie, D.; Wei, J.; Lefticariu, L.; Xu, S. A GIS-based model of potential groundwater yield zonation for a sandstone aquifer in the Juye Coalfield, Shangdong, China. *J. Hydrol.* **2017**, *557*, 434–447. [[CrossRef](#)]
33. Arulbalaji, P.; Padmalal, D.; Sreelash, K. GIS and AHP techniques Based Delineation of Groundwater Potential Zones: A case study from southern Western Ghats, India. *Sci. Rep.* **2019**, *9*, 2082. [[CrossRef](#)] [[PubMed](#)]
34. Sahu, U.; Wagh, V.; Mukate, S.; Kadam, A.; Patil, S. Applications of geospatial analysis and analytical hierarchy process to identify the groundwater recharge potential zones and suitable recharge structures in the Ajani-Jhiri watershed of north Maharashtra, India. *Groundw. Sustain. Dev.* **2022**, *17*, 100733. [[CrossRef](#)]
35. Priya, U.; Iqbal, M.A.; Abdus Salam, M.; Nur-E-Alam, M.; Uddin, M.F.; Islam, A.T.; Sarkar, S.K.; Imran, S.I.; Eh Rak, A. Sustainable Groundwater Potential Zoning with Integrating GIS, Remote Sensing, and AHP Model: A Case from North-Central Bangladesh. *Sustainability* **2022**, *14*, 5640. [[CrossRef](#)]
36. Peel, M.C.; Finlayson, B.L.; McMahon, T.A. Updated world map of the Koppen & Geiger climate classification. *Hydrol. Earth Syst. Sci.* **2007**, *11*, 1633–1644. [[CrossRef](#)]
37. Youssef, A.M.; Abu-Abdullah, M.M.; Abu AlFadail, E.; Skilodimou, H.D.; Bathrellos, G.D. The devastating flood in the arid region a consequence of rainfall and dam failure: Case study, Al-Lith flood on 23th November 2018, Kingdom of Saudi Arabia. *Z. Geomorphol.* **2021**, *63*, 115–136. [[CrossRef](#)]
38. Youssef, A.M.; Pradhan, B.; Sefry, S.A. Flash flood susceptibility assessment in Jeddah city (Kingdom of Saudi Arabia) using bivariate and multivariate statistical models. *Environ. Earth Sci.* **2016**, *75*, 12. [[CrossRef](#)]
39. Subyani, A.M. Hydrologic behavior and flood probability for selected arid basins in Makkah area, western Saudi Arabia. *Arab. J. Geosci.* **2011**, *4*, 817–824. [[CrossRef](#)]
40. Alshehri, F.; Sultan, M.; Karki, S.; Alwagdani, E.; Alsefry, S.; Alharbi, H.; Sahour, H.; Sturchio, N. Mapping the Distribution of Shallow Groundwater Occurrences Using Remote Sensing-Based Statistical Modeling over Southwest Saudi Arabia. *Remote Sens.* **2020**, *12*, 1361. [[CrossRef](#)]
41. Sulaiman, A.; Elawadi, E.; Mogren, S. Gravity interpretation to image the geologic structures of the coastal zone in al Qunfudhah area, southwest Saudi Arabia. *Geophys. J. Int.* **2018**, *2143*, 1623–1632. [[CrossRef](#)]
42. O’Callaghan, J.F.; Mark, D.M. The extraction of drainage networks from digital elevation data. *Comput. Vis. Graph. Image Process.* **1984**, *28*, 323–344. [[CrossRef](#)]
43. Strahler, A.N. Quantitative analysis of watershed geomorphology. *Trans. Amer. Geophys. Union.* **1957**, *38*, 913–920. [[CrossRef](#)]
44. Strahler, A.N. Quantitative Geomorphology of Drainage Basins and Channel Networks. In *Handbook of Applied Hydrology*; Chow, V.T., Ed.; McGraw Hill Book Company: New York, NY, USA, 1964; Section 4II.
45. Eastman, J.R.; Jin, W.; Kyem, A.K.P.; Toledano, J. Raster procedure for multi-criteria/multi-objective decisions. *Photogramm. Eng. Remote Sens.* **1995**, *61*, 539–547.
46. Kia, M.B.; Pirasteh, S.; Pradhan, B.; Mahmud, A.R.; Sulaiman, W.N.A.; Moradi, A. An artificial neural network model for flood simulation using GIS: Johor River Basin, Malaysia. *Environ. Earth Sci.* **2012**, *67*, 251–264. [[CrossRef](#)]
47. Das, S. Geospatial mapping of flood susceptibility and hydro-geomorphic response to the floods in Ulhas basin, India. *Remote Sens. Appl. Soc. Environ.* **2019**, *14*, 60–74. [[CrossRef](#)]

48. Liuzzo, L.; Sammartano, V.; Freni, G. Comparison between Different Distributed Methods for Flood Susceptibility Mapping. *Water Resour. Manag.* **2019**, *33*, 3155–3173. [CrossRef]
49. Botzen, W.; Aerts, J.; van den Bergh, J. Individual preferences for reducing flood risk to near zero through elevation. *Mitig. Adapt. Strateg. Glob. Chang.* **2013**, *18*, 229–244. [CrossRef]
50. Tehrany, M.S.; Pradhan, B.; Jebur, M.N. Flood susceptibility mapping using a novel ensemble weights-of-evidence and support vector machine models in GIS. *J. Hydrol.* **2014**, *512*, 332–343. [CrossRef]
51. Zhu, Q.; Abdelkareem, M. Mapping groundwater potential zones using a knowledge-driven approach and GIS analysis. *Water* **2021**, *13*, 579. [CrossRef]
52. Rahman, M.; Ningsheng, C.; Islam, M.M.; Dewan, A.; Iqbal, J.; Washakh, R.M.A.; Shufeng, T. Flood Susceptibility Assessment in Bangladesh Using Machine Learning and Multi-criteria Decision Analysis. *Earth Syst. Environ.* **2019**, *3*, 585–601. [CrossRef]
53. Masoudian, M. The Topographical Impact on Effectiveness of Flood Protection Measures. Ph.D. Thesis, Faculty of Civil Engineering, Kassel University, Kassel, Germany, 2009. Available online: <https://books.google.co.jp/books?hl=zh-TW&lr=&id=JQuc15e5ukEC&oi=fnd&pg=PA72&dq=The+Topographical+Impact+on+Effectiveness+of+Flood+Protection+Measures.+Ph.D.+Thesis.+Faculty+of+Civil+Engineering,+Kassel+University:+Kassel,+Germany,+2009&ots=f-N5ezRQFV&sig=nOMXpD6Fr0yR42qedBCZdIPxS9M#v=onepage&q&f=false> (accessed on 10 December 2013).
54. Bapalu, G.V.; Sinha, R. GIS in Flood Hazard Mapping: A Case Study of Kosi River Basin, India. 2005. Available online: [https://www.researchgate.net/profile/Rajiv-Sinha-2/publication/200004867\\_GIS\\_in\\_Flood\\_Hazard\\_Mapping\\_a\\_case\\_study\\_of\\_Kosi\\_River\\_Basin\\_India/links/0046353bd6f9186023000000/GIS-in-Flood-Hazard-Mapping-a-case-study-of-Kosi-River-Basin-India.pdf](https://www.researchgate.net/profile/Rajiv-Sinha-2/publication/200004867_GIS_in_Flood_Hazard_Mapping_a_case_study_of_Kosi_River_Basin_India/links/0046353bd6f9186023000000/GIS-in-Flood-Hazard-Mapping-a-case-study-of-Kosi-River-Basin-India.pdf) (accessed on 8 November 2014).
55. Benjmel, K.; Amraoui, F.; Boutaleb, S.; Ouchchen, M.; Tahiri, A.; Touab, A. Mapping of groundwater potential zones in crystalline terrain using remote sensing, GIS techniques, and multicriteria data analysis (case of the Ighremregion, western Anti-Atlas, Morocco). *Water* **2020**, *12*, 471. [CrossRef]
56. Pham, B.T.; van Phong, T.; Nguyen, H.D.; Qi, C.; Al-Ansari, N.; Amini, A.; Ho, L.S.; Tuyen, T.T.; Yen, H.P.H.; Ly, H.; et al. A Comparative Study of Kernel Logistic Regression, Radial Basis Function Classifier, Multinomial Naïve Bayes, and Logistic Model Tree for Flash Flood Susceptibility Mapping. *Water* **2020**, *12*, 239. [CrossRef]
57. Cao, C.; Xu, P.; Wang, Y.; Chen, J.; Zheng, L.; Niu, C. Flash Flood Hazard Susceptibility Mapping Using Frequency Ratio and Statistical Index Methods in Coalmine Subsidence Areas. *Sustainability* **2016**, *8*, 948. [CrossRef]
58. Janizadeh, S.; Avand, M.; Jaafari, A.; Phong, T.; Bayat, M.; Ahmadisharaf, E.; Prakash, I.; Pham, P.; Lee, S. Prediction Success of Machine Learning Methods for Flash Flood Susceptibility Mapping in the Tafresh Watershed, Iran. *Sustainability* **2019**, *11*, 5426. [CrossRef]
59. Jebur, M.N.; Pradhan, B.; Tehrany, M.S. Optimization of landslide conditioning factors using very high-resolution airborne laser scanning (lidar) data at catchment scale. *Remote Sens. Environ.* **2014**, *152*, 150–165. [CrossRef]
60. Moore, I.D.; Grayson, R.B.; Ladson, A.R. Digital terrain modelling: A review of hydrological, geomorphological, and biological applications. *Hydrol. Process.* **1991**, *5*, 3–30. [CrossRef]
61. Brooks, H.E.; Stensrud, D.J. Climatology of heavy rain events in the United States from hourly precipitation observations. *Mon. Weather Rev.* **2000**, *128*, 1194–1201. [CrossRef]
62. Nyarko, B.K. Application of a rational model in GIS for flood risk assessment in Accra. *J. Spatial Hydrol.* **2002**, *2*, 1–14.
63. Paul, G.C.; Saha, S.; Hembram, T.K. Application of the GIS-Based Probabilistic Models for Mapping the Flood Susceptibility in Bansloi Sub-basin of Ganga-Bhagirathi River and Their Comparison. *Remote Sens. Earth Syst. Sci.* **2019**, *2*, 120–146. [CrossRef]
64. Mukherjee, I.; Singh, U.K. Delineation of groundwater potential zones in a drought-prone semi-arid region of East India using GIS and analytical hierarchical process techniques. *Catena* **2020**, *194*, 104681. [CrossRef]
65. Mahmood, S.; Atta-ur, Rahman. Flash flood susceptibility modeling using geo-morphometric and hydrological approaches in Panjkora Basin, Eastern Hindu Kush, Pakistan. *Environ. Earth Sci.* **2019**, *78*, 43. [CrossRef]
66. Islam, M.M.; Sado, K. Flood hazard assessment in Bangladesh using NOAA AVHRR data with geographical information system. *Hydrol. Process.* **2000**, *14*, 605–620. [CrossRef]
67. Sharma, T.P.P.; Zhang, J.; Khanal, N.R.; Pradhan, F.A.; Nanzad, L.; Zhang, D.; Nepal, P. A Geomorphic Approach for Identifying Flash Flood Potential Areas in the East Rapti River Basin of Nepal. *ISPRS Int. J. Geo-Inf.* **2021**, *10*, 247. [CrossRef]
68. Bui, D.; Ngo, P.; Pham, T.; Jaafari, A.; Minh, N.; Hoa, P.; Samui, P. A novel hybrid approach based on a swarm intelligence optimized extreme learning machine for flash flood susceptibility mapping. *Catena* **2019**, *179*, 184–196. [CrossRef]
69. Miraki, S.; Zanganeh, S.H.; Chapi, K.; Singh, V.P.; Shirzadi, A.; Shahabi, H.; Pham, B.T. Mapping groundwater potential using a novel hybrid intelligence approach. *Water Resour. Manag.* **2019**, *33*, 281–302. [CrossRef]
70. Chorley, R.; Malm, D.; Pogorzelski, H. A new standard for estimating basin shape. *Am. J. Sci.* **1957**, *255*, 138–141. [CrossRef]
71. Withanage, N.S.; Dayawansa, N.D.K.; De Silva, R.P. Morphometric analysis of the Gal Oya river Basin using spatial data derived from GIS. *Trop. Agric. Res.* **2014**, *26*, 175–188. [CrossRef]
72. Safarina, A.B.; Karnisah, I.; Permana, A.S. Study of the effect of river basin morphology change on threshold parameters in cimahi flood early warning system. In Proceedings of the 11th Aceh International Workshop and Expo on Sustainable Tsunami Disaster Recovery, Banda Aceh, Indonesia, 10–12 October 2018.
73. Schumm, S.A. Evaluation of drainage systems and slopes in badlands at Perth Amboy, New Jersey. *Bull. Geol. Soc. Am.* **1956**, *67*, 597–646. [CrossRef]

74. Miller, V.C. A Quantitative Geomorphic Study of Drainage Basin Characteristics on the Clinch Mountain Area, Virginia and Tennessee, Project NR 389–402. In *Technical Report 3*; Department of Geology, ONR, Columbia University: New York, NY, USA, 1953.
75. Horton, R.E. Drainage-basin characteristics. *Trans. Am. Geophys. Union* **1932**, *13*, 350–361. [[CrossRef](#)]
76. Faniran, A. The index of drainage intensity—A provisional new drainage factor. *Aust. J. Sci.* **1968**, *31*, 328–330.
77. Davis, J.C. *Statics and Data Analysis in Geology*; Wiley: New York, NY, USA, 1975.
78. Abdalla, F.; Al-Turki, A.; Al Amri, A. Evaluation of Groundwater Resources in the Southern Tihama Plain, Saudi Arabia. *Arabian Journal of Geosciences—published by Springer Berlin/Heidelberg. Arab. J. Geosci.* **2015**, *8*, 3299–3310. [[CrossRef](#)]
79. Santangelo, N. Geomorphological Contribution to Flash Floods Hazard Evaluation: Examples from Campania (Southern Italy). *J. Environ. Sci. Allied Res.* **2019**, *2*, 44–50.
80. Elewa, H.H.; Qaddah, A.A. Groundwater potentiality mapping in the Sinai Peninsula, Egypt, using remote sensing and GIS-watershed-based modeling. *Hydrogeol. J.* **2011**, *19*, 613–628. [[CrossRef](#)]
81. Abdelkareem, M.; Abdalla, F. Revealing potential areas of water resources using integrated remote-sensing data and GIS-based analytical hierarchy process. *Geocarto Int.* **2021**, 1–25. [[CrossRef](#)]